Hybrid positron detection and optical coherence tomography system: design, calibration, and experimental validation with rabbit atherosclerotic models

Daqing Piao
University of Connecticut
Electrical and Computer Engineering Department
Storrs, Connecticut 06269

Mehran M. Sadeghi
Jiasheng Zhang
Yale University School of Medicine
and
VA Connecticut Healthcare System
Department of Internal Medicine
New Haven, Connecticut 06510

Yueli Chen
University of Connecticut
Electrical and Computer Engineering Department
Storrs, Connecticut 06269

Albert J. Sinusas
Yale University School of Medicine
Department of Internal Medicine
Diagnostic Radiology
New Haven, Connecticut 06510

Quing Zhu
University of Connecticut
Electrical and Computer Engineering Department
Storrs, Connecticut 06269
E-mail: zhu@engr.uconn.edu

Abstract. We evaluate the performance of our novel hybrid optical coherence tomography (OCT) and scintillating probe, demonstrate simultaneous OCT imaging and scintillating detection, and validate the system using an atherosclerotic rabbit model. Preliminary data obtained from the rabbit model suggest that our prototype positron probe detects local uptake of fluorodeoxyglucose (FDG) labeled with ^{18}F positron (beta) radionuclide emitter, and the high-uptake regions correlate with sites of injury and extensive atherosclerosis areas. Preliminary data also suggest that coregistered high-resolution OCT images provide imaging of detailed plaque microstructures, which cannot be resolved by positron detection. [DOI: 10.1117/1.1954773]

Keywords: biomedical optics; radiation; imaging systems; coherent optical systems.

Paper 04135RR received Jul. 15, 2004; revised manuscript received Feb. 14, 2005; accepted for publication Feb. 28, 2005; published online Jul. 15, 2005.

1 Introduction

Conventional noninvasive scintigraphic techniques such as single photon emission computed tomography (SPECT) and positron emission tomography (PET) make use of radiolabeled molecules (radiotracers) designed to specifically target individual metabolic or enzymatic activities involved in a particular molecular process. These techniques have the ability to detect and serially monitor a variety of biological and pathophysiological processes, usually with tracer quantities of radiolabeled peptides, drugs, and other molecules at doses free of pharmacologic side effects.[1] This allows the imaging of biological processes *in vivo* with high specificity. However, SPECT and PET provide limited image resolution, and their sensitivity is too low to detect most atherosclerotic plaques. Therefore, a number of investigators are developing intravascular radiation detection systems for detection of atherosclerosis.[2–8] Compared with external imaging, intravascular approaches have the significant advantage of detecting localized small lesions that might involve endothelial cells or underlying structures. These intravascular systems offer improved sensitivity for detection of small amounts of radioactivity, although spatial resolution is limited.

Inflammatory cell activity is increased in vulnerable plaques, and plaque inflammation can be detected with fluorodeoxyglucose (FDG) labeled with ^{18}F positron (beta) radionuclide emitter (^{18}FDG), a marker of metabolism.[2,9] The half life (110 min) of ^{18}F is relatively long compared to other positron emission tracers. The strength of scintigraphy is to evaluate the functional status of the plaque, rather than its anatomy. Therefore, additional information about the plaque will be obtained, which is not feasible with current anatomic imaging-based technologies, such as intravascular ultrasound (IVUS).

Address all correspondence to Quing Zhu, ECE, University of Connecticut, 371 Fairfield Road, U1157, Storrs, CT 06269. Tel: 860–486–5523; Fax: 860–486–2447; E-mail: zhu@engr.uconn.edu

1083-3668/2005/10(4)/044010/10/$22.00

Most catheter-based radiotracer detection systems have focused on beta detection of positron emitting tracers using scintillating plastic fibers. Since the targeted cardiac vessels have diameters of less than 5 mm, they correspond well with the tissue path length (~3 mm) for beta particles with energies of >600 keV. The catheter designed by Patt et al. in Ref. 5 employs 0.5-mm-diam scintillating fibers. ^{18}F labeled tracers have been developed for other targets such as the alpha-v beta-3 integrin, which may be upregulated in remodeling arteries. Although the detection of unstable or vulnerable atherosclerotic plaque will be enhanced by targeting more specific markers, this work is focused on demonstration of targeted detection using FDG labeled with ^{18}F positron (beta+) radionuclide emitter.

Optical coherence tomography (OCT) can reveal structures within the body to several millimeters in depth with unprecedented resolution on the order of 3 to 15 μm,[10–13] which is an order of magnitude higher than conventional IVUS. Recent *ex vivo* studies reported in Refs. 13–18 have demonstrated that intravascular OCT can differentiate lipids from nonlipids, identify the intima over the lipid collection, and quantify macrophages through signal processing. *In vivo*, fibrous, lipid-rich coronary plaques, calcifications, and intimal hyperplasia were identified.[19] Characteristics of various plaque components have been established by *ex vivo* histological correlation, highlighting a sensitivity and specificity of 92 and 94%, respectively, for lipid-rich plaque; 95 and 100% for fibrocalcific plaque; and 87 and 97% for fibrous plaque.[15] OCT provides high-resolution imaging of intravascular structures; however, it has limited functional imaging capability. OCT has been demonstrated to be capable of visualizing macrophages,[18] but the ability of OCT to assess macrophage activity is currently unknown. Recent research activities on improving OCT functional imaging capabilities include polarization sensitive OCT,[20–22] Doppler blood flow OCT,[23–27] contrast enhanced OCT,[28,29] spectroscopy OCT,[30] combing OCT with fluorescence spectroscopy,[31] etc.

We have demonstrated the principle of a novel hybrid catheter-based device, which integrates an OCT probe and scintillating fibers for dual-modality high resolution structural and high-sensitivity functional imaging.[32] In this work, we evaluate the performance of our improved hybrid OCT and scintillating probe, demonstrate simultaneous OCT imaging and scintillating detection, and validate the system using an atherosclerotic rabbit model. Preliminary data obtained from the rabbit model suggest that our prototype positron probe detects local ^{18}FDG uptake, and the high-uptake regions correlate with sites of injury and atherosclerotic plaques. Preliminary data also suggest that coregistered high resolution OCT images provide imaging of detailed plaque microstructures, which cannot be resolved by positron detection.

2 System Design

The improved prototype of a beta-OCT imaging system is shown schematically in Fig. 1. The system consists of 1. a beta detection system, 2. an OCT imager and catheter probe, 3. a combined beta-OCT probe enclosed in a light-tight box, and 4. a computer for control and data acquisition. The first three units are described in detail in the following sections.

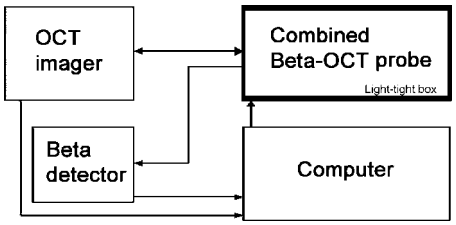

Fig. 1 Schematic of the combined beta-OCT imaging system.

2.1 *Beta Detection System*

The beta detection system is a catheter-based single-channel positron imaging unit prototyped as shown in Fig. 2. It consists of a plastic scintillating fiber, clear light guide, photomultiplier tube (PMT), and PC-based multichannel analyzer (MCA). The plastic scintillating fiber is a 1-mm-diam Bicron BCF-12 blue-emitting fiber. The BCF-12 blue scintillator has an emission peak at 435 nm, decay time of 3.2 ns, 1/e attenuation length greater than 2.2 m, and photon generation of ~8000/MeV. The scintillating fiber was polished and glued to a clear light guide of the same diameter and 0.75 m lengths. The scintillating fiber and the clear light guide were connected using regular glass cement. The light attenuation of this fiber junction was measured to be 0.25 dB, which was minimal. The scintillating fiber was then cleaved to make a 2-mm tip, which compromises resolution and signal-to-noise ratio (SNR), as discussed in our earlier work.[32] In the next prototype that we are planning to develop, the scintillating fiber will be fused with the regular optical fiber to reduce the coupling lose at the junction, and the distal surface of the scintillating fiber will be coated with reflective paint to further improve the scintillation collection. A light-tight rubber sleeve encloses the entire light guide, and the distal part of the light guide has an extra sleeve made with 120-mm-long 16-gauge stainless steel needle body. The stainless steel sleeve is mounted to a homemade three-way translation stage. The proximal end of the clear light guide is attached against the PMT window through a light-tight aluminum box, which en-

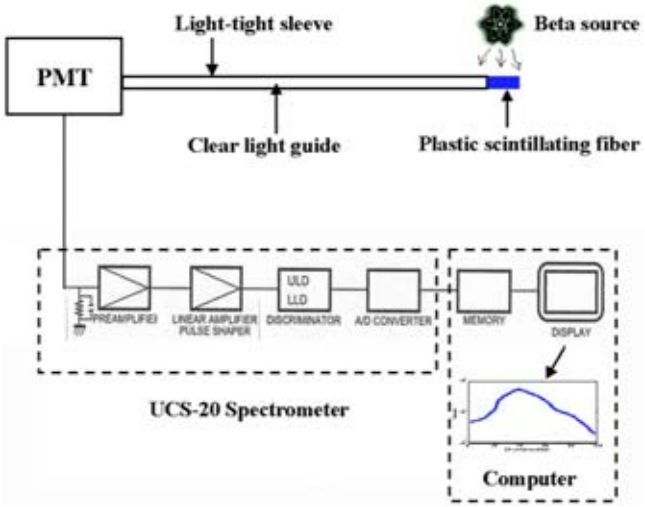

Fig. 2 Schematic of the beta detector.

closes the PMT and a negative high-voltage power supply. The Hamamatsu R2949 PMT was selected for its high sensitivity, low dark current, and convenient side-on window. The wavelength of maximum response of R2949 is at 400 nm, well fitted for detecting the blue light emitted from the BCF-12 scintillating fiber. The PMT anode output is directly connected to the preamplifier input of a UCS-20 Spectrometer (Spectrum Techniques, Inc., Oak Ridge, TN). UCS-20 is a PC-based multichannel analyzer (MCA) featuring a maximum of 2048 channels. The communication between the UCS-20 and the computer is via the standard USB cable. UCS-20 includes an internal charge-sensitive preamplifier, computer-controlled linear amplifier for pulse shaping, lower level discriminator (LLD), upper level discriminator (ULD), analog-to-digital (A/D) converter, and positive 0 to 2500 V high voltage power supply. The software provides three modes of photon counting: pulse height analysis (PHA), multichannel scaling (MCS), and Mossbauer.

2.2 *OCT Imager*

The details of the OCT imager [shown in Fig. 3(a)] can be found elsewhere.[26] In brief, a superluminescent diode (SLD) is used as the low-coherence source. The SLD has a peak wavelength at 1300 nm, and spectrum bandwidth of 40 nm. The coherence length of this SLD is 18.6 μm. The reference arm consists of a grating-based time-domain scanning optical delay line[33] [not shown in Fig. 3(a)]. In the sample arm, we have designed a prototype rotating catheter probe 2 mm in diameter to perform intravascular circumferential OCT imaging [see Fig. 3(b) for the size of the probe]. In the detection arm, balanced configuration is used to suppress the source intensity noise.[34]

We have designed and had OZ Optics fabricate a 1.6 -mm-diam OCT catheter as shown in Fig. 3(b). The catheter body is composed of a flexible, rotary inner sleeve that fits loosely inside a homemade stationary outer sheath. The catheter body is made flexible to allow for bending during passage through the contours of blood vessels. The outer sheath allows the inner sleeve to rotate freely and provides a smooth exterior for passage through internal organ systems. The inner sleeve is connected to a FC/PC connector at the proximal end and to the distal optics at the other end. The optical fiber is fixed within the center of the inner sleeve. Rotational torque exerted at the proximal end of the inner sleeve by the drive mechanism is transported to the distal end to rotate the beam focusing/directing optical components.

The distal end of the catheter is composed of miniature beam focusing and directing optics. The single-mode fiber is attached to a gradient-index (GRIN) lens. A microprism is mounted at the distal surface of the GRIN lens to direct the beam perpendicular to the axis of the catheter. A homemade transparent cap is added on to enclose the distal end of the catheter for waterproof purposes. Due to the cap, the size of the catheter tip increases to 2.0 mm. The microprism, the GRIN lens, the inner sleeve, the optical fiber, and the proximal rotating optical connector are all attached with optical cement to form a single unit, the rotating shaft portion of the catheter. The GRIN lens is 1.0 mm in diameter, and the microprism has a 1-mm edge length. The predicted spot size is 30 to 35 μm at a working distance of 2 mm from the prism

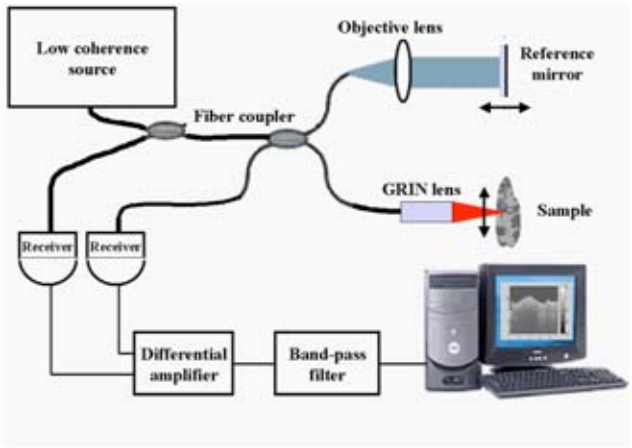

Fig. 3 (a) Schematic of the OCT imager. The OCT is configured with balanced detection. (b) Picture of the prototype rotating OCT catheter probe. The structure of the probe is sketched beside the actual probe. A U.S. dime is placed nearby for size comparison.

output surface. During image acquisition, the catheter is inserted into the blood vessel being imaged, and as the drive motor turns, the shaft of the catheter and the distal optics circumferentially scan the focused beam perpendicular to the axis of the catheter. The speed of imaging depends on the speed of the rotation and the OCT unit acquisition speed.

The light coupling mechanism from the interferometer to the rotary catheter is similar to that reported in Ref. 35. Incident light from a fixed single-mode optical fiber is coupled using an optical fiber FC/PC adaptor into the single-mode fiber of the catheter. FC connectors mounting to the FC/PC adaptor ensures precise alignment and optical coupling between the fixed and rotating fibers. The input fiber connector is fixed to the FC/PC adaptor, while the locking notch of the catheter fiber connector is removed for free rotation. The drive assembly of the catheter is mounted with the FC/PC adaptor enclosed. The FC/PC adaptor is attached to a hollow rotary stage through a shaft assembly, and the rotary stage is connected to a dc motor through a timing belt pulley.

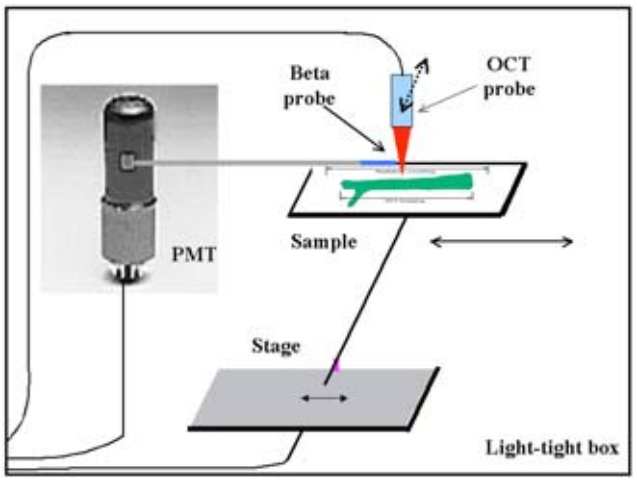

Fig. 4 The combined beta-OCT probe enclosed in a light-tight aluminum box.

2.3 *Combined Beta-OCT Probe*

We have constructed a coregistered beta/OCT imaging probe. The OCT catheter passes into a light-tight box through a small hole, and the distal end of the catheter is confined side by side with the beta probe. The OCT catheter-driving assembly is mounted to a motorized linear stage, which renders image localization by pulling the combined beta/OCT probe rather than moving the sample.[32] Using this setup, we have acquired coregistered OCT and beta detection data from freshly excised pieces of bovine coronary arteries. Results are reported in Sec. 3.2.

For experiments using atherosclerosis rabbit models, we did not perform an intravascular study but modified the hybrid probe to scan the open vessel to preserve the artery for beta autoradiography. This ensured that the probe did not touch the endothelial layer. The combined beta/OCT probe was positioned above the vessel and was aligned parallel to the long axis of the sample (see Fig. 4). The OCT probe, or the GRIN lens described in Sec. 2.2, was deployed vertically beside the beta probe. The OCT probe scanned transversely across the vessel, and the stationary beta probe detected the local beta activity. The sample was translated parallel to the scintillating fiber axis after each coregistered beta-OCT scan.

Beta particle detection requires single-photon counting, where the ambient light level should be minimized. Therefore all of the light-sensitive components, including the scintillating fiber, light guide, and PMT, must be enclosed in a light-tight box. Because of the coregistered beta-OCT imaging configuration, the light-tight box must also accommodate the OCT probe. We have constructed a light-tight box, and repeated testing with the sealed source has shown that in using this light-tight box, the maximum counting and the background level show no significant difference for operation in a dark or light room.

2.4 *Rabbit Preparation*

To validate the proposed hybrid intravascular OCT/scintillator catheter, we have conducted experiments with an atherosclerotic rabbit model. New Zealand White (NZW) rabbits weighing 3 to 3.5 kg (Charles-River Laboratories, Wilmington, Massachusetts) were maintained on a high cholesterol (1% cholesterol) diet. One week following initiation of the high-fat diet, rabbits were anesthetized with ketamine (30 mg/Kg) and xylazine (3 mg/Kg) i.p., and a 5F sheath was inserted into the left carotid artery under fluoroscopy. An angioplasty balloon catheter (3.0×20 mm, Cordis, Johnson and Johnson Company) was passed over wire to the distal abdominal aorta, and was inflated to 10 atmosphere for 1 min. The abdominal artery was injured three times. Subsequently, the catheter was removed, the external carotid artery ligated, and the wound closed. Rabbits were continued on the hyperlipidemic diet for 6 months before imaging experiments. Experiments were performed according to the regulations of Yale University's Animal Care Committee.

3 Results

3.1 *Testing and Calibration of the Beta Detection System*

The performance of the OCT system has been demonstrated elsewhere.[26,27,32] In this part, we present the testing and calibration results of the beta detection system.

FDG labeled with ^{18}F is the most commonly used radiopharmaceutical in positron emission nuclear imaging. However, ^{18}FDG is inconvenient for use as a calibration source due to its preparation, transportation, and relatively short half life for repeated calibration purposes. Instead, we have used a sealed 0.7-μCi thallium TI-204 isotope with a half life of 3.77 years for most calibration tests presented in this work.

Several critical system parameters related to the *ex vivo* and *in vivo* use of this scintillating catheter were evaluated experimentally. These parameters are signal-to-background ratio versus multichannel analyzer (MCA) lower level discriminator (LLD) setup, minimal counting time, detection sensitivity, and ratio of probe response to beta and gamma.

3.1.1 *Signal-to-background ratio versus MCA LLD setup*

The PMT dark noise spectrum[36] measured with minimum LLD is shown in Fig. 5(a) (the solid curve). The dashed curve in Fig. 5(a) is the measured gross beta spectrum when the TI-204 source is placed 1 mm away from the beta probe. The pure beta spectrum (dotted curve) obtained by subtracting the background from the gross counting shows a continuous energy distribution up to a definite maximum[37] that corresponds to 765 keV for TI-204 beta emission.

The signal-to-background ratio (SBR) may be calculated from the total counts of TI-204 source relative to the background counts. The dependence of SBR to the LLD of MCA is shown in Fig. 5(b) (solid curve). It is shown that as LLD increases, SBR reaches a maximum and starts to decrease. This indicates that there is an optimum LLD setup for maximum SBR. However, the counting statistics must be taken into account for setting up the optimum LLD. As the LLD increases, the total counts decrease, resulting in an increased relative probable error (RPE)[36] that is determined by RPE $= \sqrt{N}/N$, where N is the total photon count. The RPE curve in Fig. 5(b) (dot-dashed line) is inversely plotted to show the

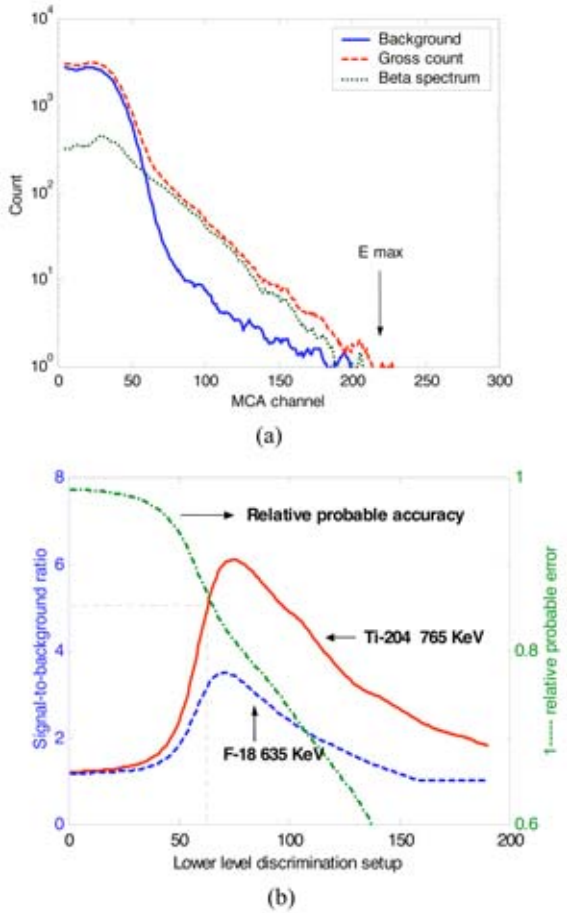

Fig. 5 Determination of LLD for optimum SBR. (a) Spectrum of TI-204 beta emission. (b) The dependence of SBR and measurement error on LLD setup.

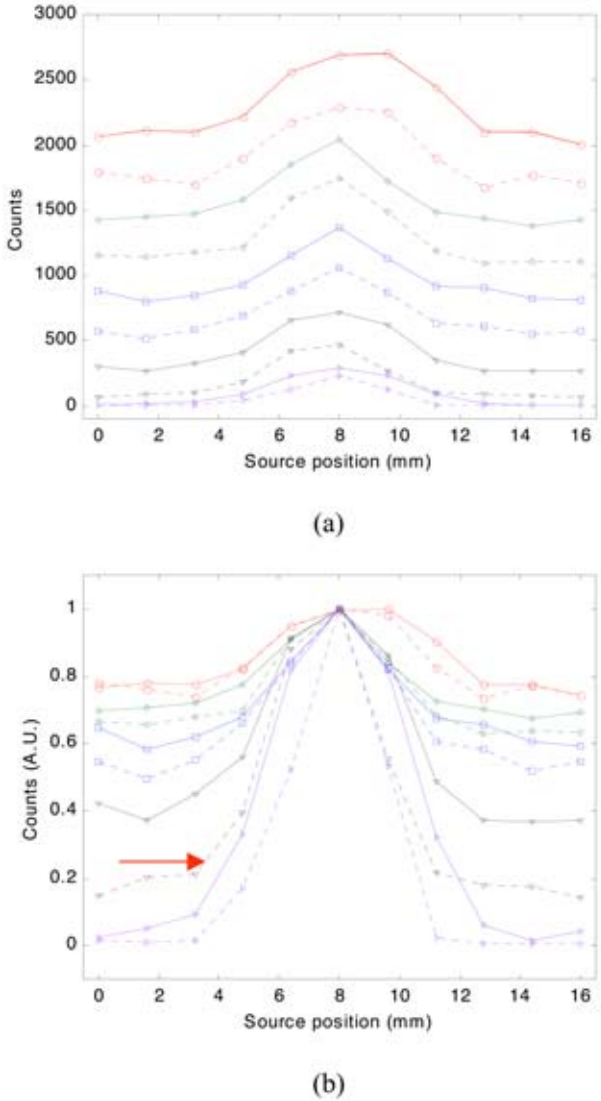

Fig. 6 Photon counting results at different LLD levels by translating the TI-204 source parallel to the beta probe axis. (a) The absolute and (b) normalized counting results.

decrease in the measurement accuracy as LLD increases. It is apparent that there is a tradeoff between SBR and RPE at a lower LLD side of the SBR maximum.

TI-204 has maximum beta decay energy of 765 keV, while ^{18}Fdeoxyglucose has maximum positron emission energy of 635 keV. If the same system is used to measure the positron radiation from ^{18}FDG, the beta spectrum maximum will shift to the lower side. The ^{18}FDG spectrum can be approximated by squeezing the TI-204 spectrum from 765 to 635 keV. This approximation is intended for assisting the determination of optimum LLD in ^{18}FDG-based photon counting. The SBR of ^{18}FDG as a function of LLD is shown in Fig. 5(b) as the dashed curve below the TI-204 SBR. The optimal LLD for approximated ^{18}FDG counting shifts to the lower side, which agrees with the fact that ^{18}FDG beta emission has lower maximum energy compared to TI-204. The finalized LLD setup indicated by the vertical dashed line intersecting with the abscissa around 60 may provide a balance between SBR and RPE for both TI-204-based counting in calibration and ^{18}FDG-based-counting in *ex vivo* and *in vivo* experiments.

Further tests were conducted to validate the dependence of SBR on the LLD setting. Shown in Fig. 6 are the photon counting results at different LLD levels by translating the TI-204 source parallel to the beta probe axis. The absolute counting results are shown in Fig. 6(a), while the normalized results are shown in Fig. 6(b). The curves from top to bottom correspond to gradually increased LLD. As LLD increases, the total counts at positions near and far from the source all decrease; nevertheless, the SBR improves gradually so that the source position is resolved better. The second dashed curve from the bottom in Fig. 6(b) corresponds to the optimal LLD determined in Fig. 5(b). It is worth mentioning that, in the source position-resolved test, each measurement curve provides a convolution between the point spread function of the 2-mm scintillating probe and the point spread function of the 4-mm source at a different LLD level.

3.1.2 *Counting time*

It is critical to reduce the counting time for *in vivo* use of the beta probe. However, a minimum counting time is needed for accuracy. Figure 7(a) shows the total events measured at dif-

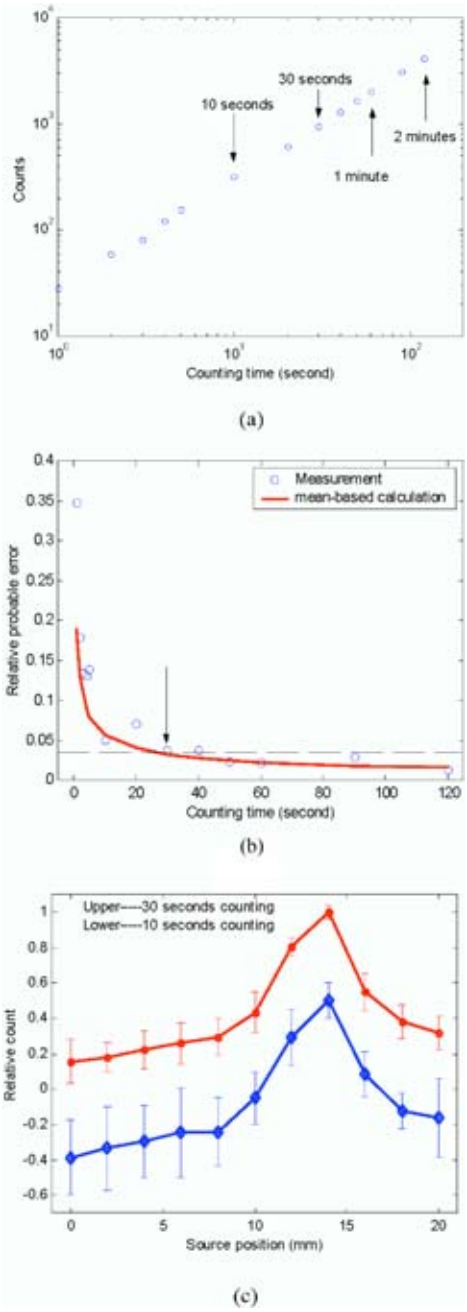

Fig. 7 Determining the counting time with the measurement error taken into account. (a) Counts versus counting time. (b) Relative probable error versus counting time. (c) Localization of the source position at 10 and 30 s counting times.

ferent counting times from 1 s to 2 min with the optimum LLD setting discussed early. Each data point was averaged for 10 repeated measurements. It shows excellent linearity between total counts and counting time. However, the counting accuracy degrades dramatically when the counting time is less than 10 s [see Fig. 7(b)]. When the counting time is not less than 30 s, the RPE remains relatively uniform. The position-resolved photon counting at counting times of 10 and 30 s, respectively, is compared in Fig. 7(c). Although the source can be resolved at both settings, the 10-s counting shows much larger measurement fluctuation than the 30-s counting. Based on these calibration tests with our current system, we choose 30 s as the counting time in the experiments thereafter.

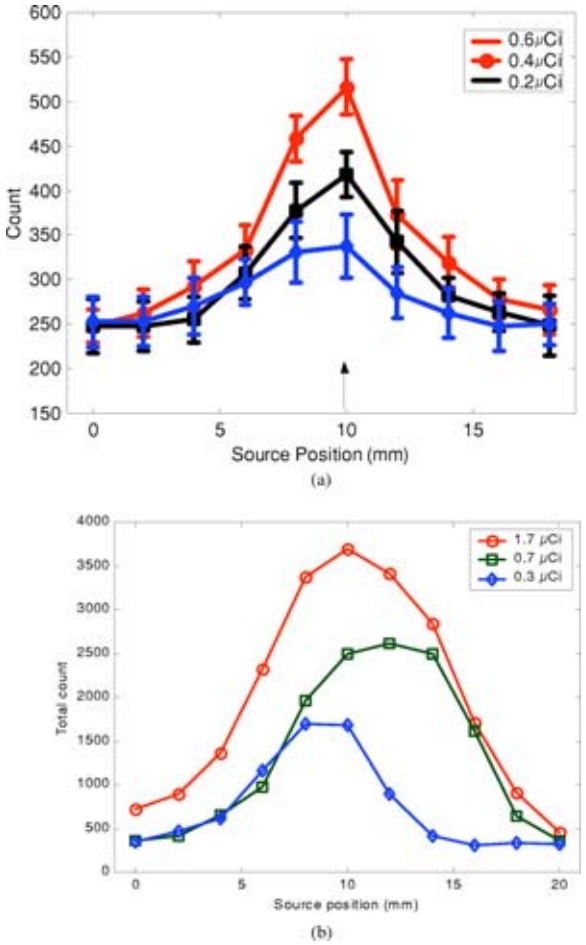

Fig. 8 Detection sensitivity test. (a) Sealed TI-204 source. (b) ^{18}FDG.

3.1.3 *Detection sensitivity*

System sensitivity was measured by placing aluminum absorbers with different density thickness over the TI-204 source. For beta emission of $E=765$ keV by TI-204, the half-thickness of aluminum is 25.4 mg/cm^2 based on Libby's equation.[38] We have used aluminum absorbers with densities of 13.8 and 34.9 mg/cm^2 to attenuate the 0.63-μCi TI-204 source, resulting in source activities of 0.43 μCi and 0.24 Ci, respectively. Shown in Fig. 8(a) are the average position-resolved results obtained from 10 sets of repeated measurements. Note that the activity of the 0.7-μCi TI-204 source was reduced to 0.63 μCi at the time when Fig. 8(a) was revised. In these tests, the source without/with an absorber was placed 1 mm away from the beta probe and the source position can be clearly resolved for a 0.24-μCi TI-source.

The detection sensitivity was also verified with different doses of ^{18}FDG [see Fig. 8(b)]. The ^{18}FDG tests were done by manually pulling the catheter backward inside a vessel. The vessel was attached to tapered tubings on each side, and the catheter was inserted up to the distal tapered tubing. The

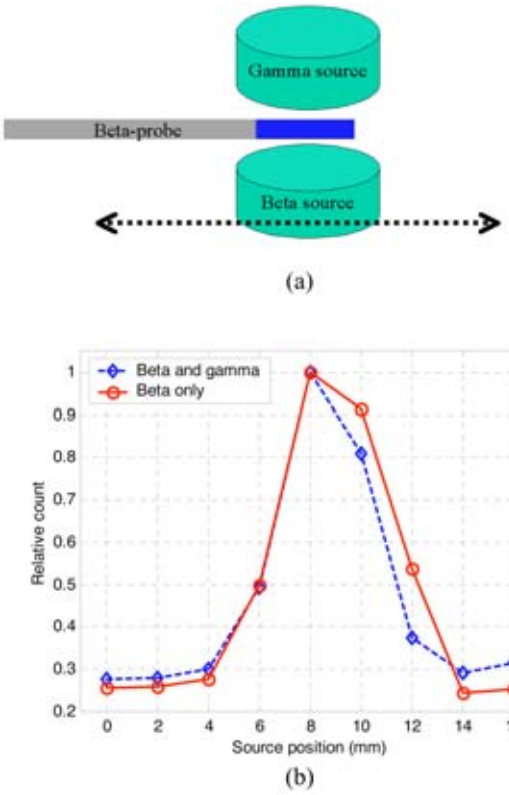

Fig. 9 The probe response to beta and gamma. (a) Testing setup. (b) SBR results.

tubings were connected to a plastic tube filled with saline water. By pulling back the catheter, we could maintain the vessel position and shape. Each time the catheter had been pulled back, we must carefully push the catheter back into the distal tubing. As shown in Fig. 8(b), three curves were aliened reasonably well in position by carefully controlling the initial position, and pulling steps that could vary for each set of measurements. As a result, a repeated measurement was not applicable for FDG tests.

3.1.4 *Ratio of probe response to beta and gamma*

The reduction of the associated gamma background is essential for *in vivo* beta imaging, especially for imaging coronary arteries. The beta/gamma ratio is measured from the SBR of TI-204 with and without the presence of gamma background. As shown in Fig. 9(a), a 0.7-μCi gamma source Cs-137 was placed 1 mm away from the beta probe at the opposite side of the TI-204 source. The activities of these gamma and beta sources are the same, and the ratio between gamma and beta energies is 662/765, close to the 511/635 of ^{18}FDG. From the SBG results with and without gamma background [see Fig. 9(b)], we have calculated the ratio of the detection response between beta and gamma, that is

$$\gamma = \frac{\text{Response\_beta}}{\text{Response\_gamma}} = \frac{\text{beta-background}}{\text{gamma-background}}.$$

The γ is found to be between 10 and 13.

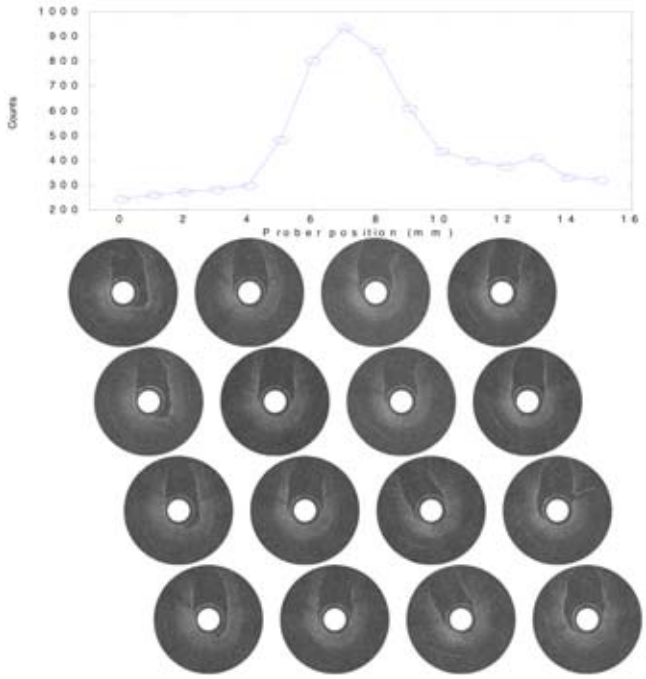

Fig. 10 Coregistered beta/OCT imaging. Top curve: beta counting. Bottom image locations: top row for 1, 5, 9, 13; row two for 2, 6, 10, 14; row three for 3, 7, 11, 15; and row four for 4, 8, 12, 16.

3.2 *Coregistered Beta/OCT Imaging Using Sealed Beta Source*

Using the coregistered beta/OCT imaging probe, we acquired coregistered OCT and beta detection data from freshly excised pieces of bovine coronary arteries. The sealed beta source is positioned close to a 3-mm-diam hole left at the artery. The examined artery is securely positioned, and an OCT cross section image and radiation counting are acquired simultaneously after each 1-mm displacement of combined probe. The acquired coregistered beta/OCT images shown in Fig. 10 are quite similar to those reported in Ref. 32, whereas the beta detection resolution is improved significantly due to shorter length of the scintillating tip and optimized counting parameters.

3.3 *Coregistered Beta/OCT Imaging Result Obtained from Injured Rabbit Models*

The injured rabbit was injected intravenously with ^{18}FDG (3.5 mCi). After one hour, the rabbit was euthanized and the entire abdominal aorta and iliac arteries were removed, cut open, and fixed to the board. Several thin pieces were cut fresh before the combined imaging for histological analysis. A photograph of the sample is shown in Fig. 11(a). The scintillating fiber tip is positioned above the sample and is aligned parallel to the long axis of the sample. The OCT probe, or the GRIN lens, is deployed vertically beside the beta probe. The OCT probe scans transversely across the vessel, and the stationary beta probe detects the local beta activity. The sample is translated parallel to the scintillating fiber axis after each beta-OCT scan. Since the half-life of ^{18}FDG is short, the radiation detection was conducted first at a step of 0.8 cm and

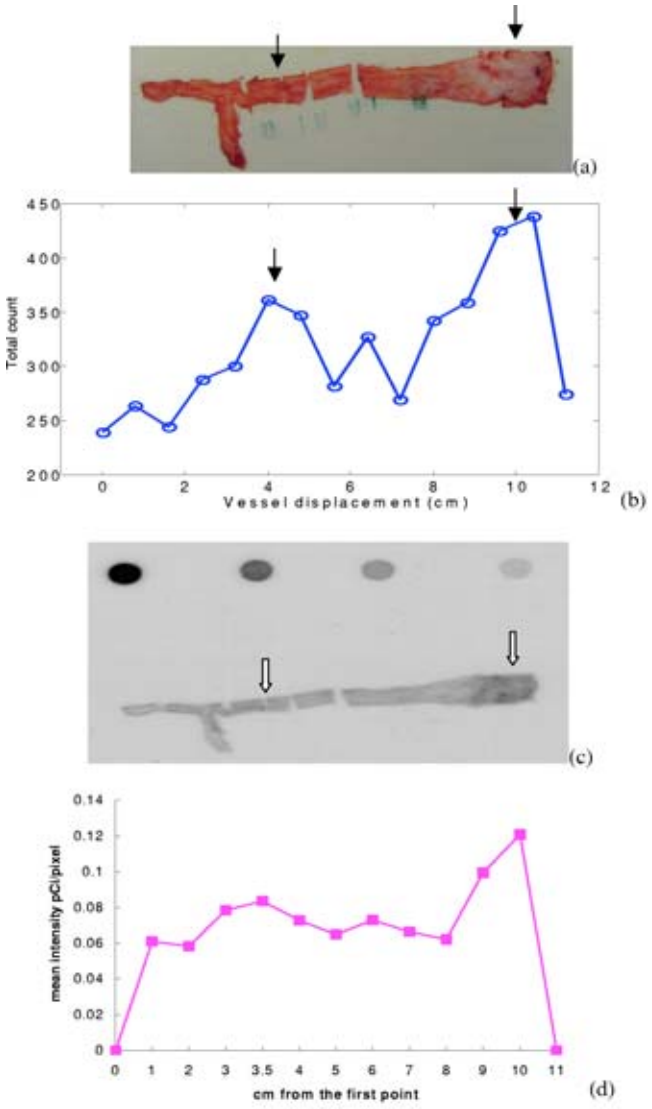

Fig. 11 (a) Photograph of the artery. (b) Detection curve obtained from the coregistered scintillating probe. The first peak from the left (marked with shot arrow) corresponds to the injured site, and the second peak from the left corresponds to the extensive atherosclerotic areas with high lipid contents. First point at 0 cm and last point at 11 cm are outside the vessel. (c) Beta autoradiography obtained with overnight exposure. (d) The mean intensity per pixel of the autoradiography.

with 30-s counting at each position. The total beta scanning time for the entire vessel was about 8 min. After beta scanning, the sample was repositioned to the origin by moving the stage, and coregistered OCT scans were acquired in 0.4-cm step. At the gap positions where no sample was underneath, OCT images were acquired in 0.2-cm step.

The detection curve obtained from a coregistered scintillating probe is shown in Fig. 11(b). The first point at 0 cm and the last point at 11 cm are outside of the vessel sample. The first peak from the left (marked with a short arrow) corresponds to the injury site, and the second peak from the left corresponds to the extensive atherosclerosis area with high lipid content (pointed by an arrow). The beta autoradiography obtained with overnight exposure is shown in Fig. 11(c). The two dark regions pointed by the white arrows from left to right correspond to the site of injury and the area of extensive atherosclerosis. The autoradiography was scanned on a high-resolution scanner (Seiko Epson Corporation). The mean intensity per pixel of the autoradiography was measured using Kodak 1D software (Eastman Kodak Company, Rochester, New York) at regular intervals along the artery, background corrected, and expressed in arbitrary numbers as shown in Fig. 11(d). Linearity of the signal was confirmed using serial dilutions of the tracer. The mean intensity curve quantitatively agrees with the detection curve shown in Fig. 11(b). The coregistered sequence of corresponding OCT images is shown in Fig. 12. In the site of injury, the lipid shadowing is pronounced, as pointed by white arrows. In the area with extensive atherosclerosis, the lipid shadowing appears again, as pointed by white arrows, and the fibrocalcific aortic plaque with very low light scattering or signal-poor interior is circled in the last figure. Similar signal-poor regions with sharply delineated upper and/or lower borders were reported in Ref. 15 with samples obtained from a human autopsy. Representative histological slices and OCT images obtained from the sites of injury and the extensive atherosclerosis are shown in Figs. 12(b) and 12(c), respectively. Histological slices were stained with Elastic Van-Gieson (EVG) at 200-fold magnification. At both the injury site and the extensive atherosclerosis regions, the intima layer was thickened and OCT images showed significant lipid shadowing.

4 Discussion and Summary

We report our optimal design and *ex vivo* validation of a novel combined OCT imaging and scintillating detection system. The optimal design regarding positron detection is based on commercially available plastic scintillators and a PMT detection system. For future *in vivo* experiments, the scintillating probe and the detection system has to be further optimized to reduce the total counting time and to improve the lesion beta-to-background tissue gamma ratio. For our current system, the reliable minimal counting time for ^{18}FDG tracers at each location is 30 s. This limitation is related to the system noise counts and can be shortened by using a cooled PMT. With the current system, several minutes are needed to screen a vessel of several centimeters. This time frame is certainly too long for this invasive procedure. The next prototype catheter design will have several pairs of scintillating fibers displaced laterally over a length of 3 to 4 cm, and the counting outputs from these locations can be read simultaneously in 30 s or less from a position sensitive PMT. Further optimization regarding lesion beta/tissue gamma detection ratio can be made by using more sensitive scintillating crystals[39] and silicon solid-state detectors[4] with optimal beta/gamma detection configuration.[8]

The reported scintillating probe has been calibrated using the sealed TI-204 beta (beta−) source on optimal LLD setting, counting time, detection sensitivity, and beta/gamma ratio. However, ^{18}FDG is a positron (beta+) emitter, which produces additional background gamma rays generated by the annihilation process of positions and electrons. Therefore, the calibrations were done under ideal conditions without background interference. The ^{18}FDG detection sensitivity tests using excised vessels filled with saline water agreed reasonably

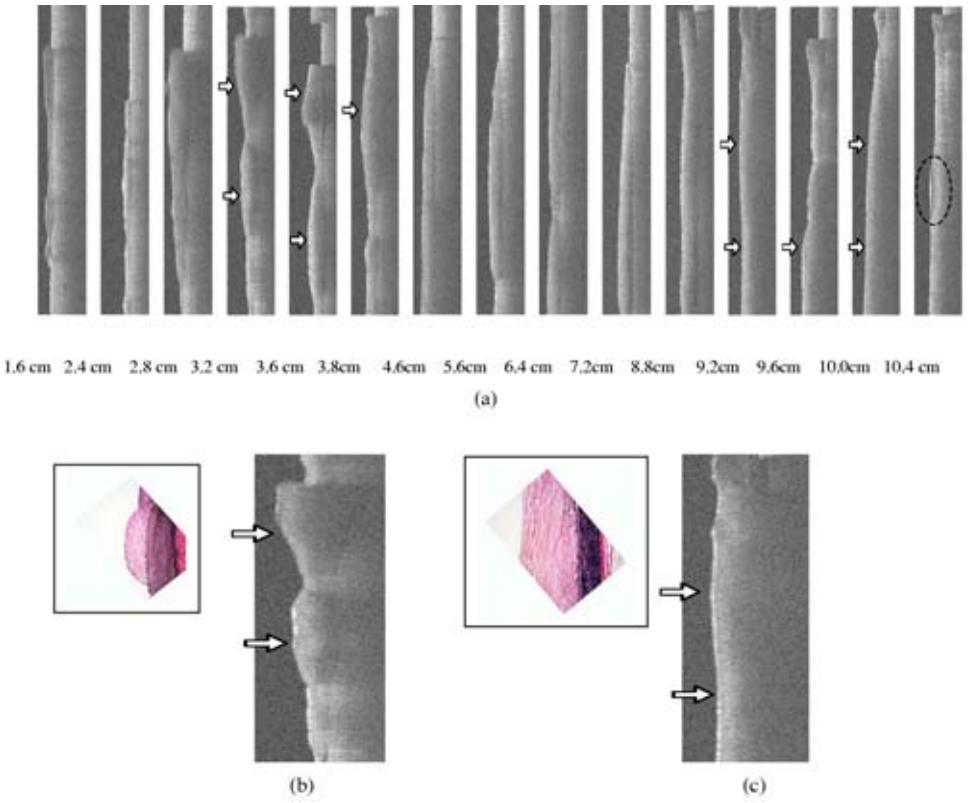

Fig. 12 Coregistered OCT images numbered from left to right. The spatial dimension from top to bottom is 4.8 mm and the depth is 2 mm. The first group of white arrows in the 3.6-cm region points to lipid shadowing regions corresponding to the injured site. The second group of white arrows in the 9.6-cm region points to lipid shadowing regions corresponding to extensive lipid content area toward the aorta. In the last figure the fibrocalcific aortic plaque is circled. (b) Representative histology (×200 magnification) and OCT image obtained from the injured site. Elastic fibers under Elastic Van-Gieson (EVG) staining appear dark and the elastic membrane was thickened compared with noninjured sites. The OCT image showed lipid shadowing with less light penetration. (c) Representative histology and OCT image obtained from extensive plaque regions. The OCT image showed significant lipid shadowing with less light penetration.

well with the sensitivity tests using TI-204. However, more realistic tests with scintillating catheters inserted into the *in vivo* atherosclerotic arteries are needed to further validate the detection sensitivity of the probe under the interference of background gamma.

In addition to background tissue gamma activity, circulating blood will contain certain amounts of beta and gamma activities and the *in vivo* total count will be the summation of blood activity, background tissue gamma activity, and local beta activity of metabolically active plaques. We anticipate that blood beta activity will be statistically uniform across the screening section of the vessel and should not limit the detection of local ^{18}FDG uptake sites. Future *in vivo* experiments are planned to assess the beta detection sensitivity with the presence of blood.

The last technical issue that needs to be addressed is the miniaturization of the hybrid catheter. For the hybrid intravascular experiment reported in Sec. 3.2, the OCT catheter 2.0 mm in diameter (counting the protection cap) and the scintillating fiber 1 mm in diameter were mounted side by side with a lateral displacement so that the OCT circumferential scanning was not blocked by the scintillating probe. The total size of the hybrid probe is more than 3 mm, which is too large for *in vivo* coronary studies. The hybrid catheter has to be reduced to less than 2 mm by further optimizing the OCT scanning assembly and incorporating pairs of 0.25-mm- to 0.5-mm-diam scintillating fibers.

In summary, feasibility studies obtained from the rabbit model suggest that our prototype positron probe detects local ^{18}FDG uptake, and the high uptake regions correlate with sites of injury and extensive atherosclerosis. Preliminary data also suggest that coregistered high resolution OCT images provide detailed plaque microstructures, which cannot be resolved by positron detection.

Acknowledgment

We thank Guillermo Tearney, Massachusetts General Hospital and Harvard Medical School, for sharing his intravascular OCT experience with us, and providing valuable suggestions on using a scintillating probe for screening. We thank Martin Tornai, Departments of Radiology and Biomedical Engineering at Duke University, for valuable discussions on tissue interaction with beta− and beta+ particles.

References

1. F. G. Blankenberg and H. W. Strauss, "Nuclear medicine applications in molecular imaging," *J. Magn. Reson Imaging* **16**(4), 352–361 (2002).
2. J. H. Rudd, E. A. Warburton, T. D. Fryer, H. A. Jones, J. C. Clark, N. Antoun, P. Johnstrom, A. P. Davenport, P. J. Kirkpatrick, B. N. Arch,

J. D. Pickard, and P. L. Weissberg, "Imaging atherosclerotic plaque inflammation with [18F]-fluorodeoxyglucose position emission tomography," *Circulation* **105**(23), 2708–2711 (2002).
3. H. W. Strauss and F. G. Blankenberg, "Small is beautiful: specialty imaging devices and the growth of nuclear cardiology," *J. Nucl. Cardiol.* **7**(2), 175–179 (2000).
4. E. J. Hoffman, M. P. Tornai, M. Janecek, B. E. Patt, and J. S. Iwanczyk, "Introperative probes and imaging probes," *Eur. J. Nucl. Med.* **26**(8), 913–935 (1999).
5. B. E. Patt, J. S. Iwanczyk, L. R. MacDonald, Y. Yamaguchi, C. R. Tull, M. Janecek, E. J. Hoffman, W. Strauss, R. Tsugita, and V. Ghazarossian, "Intravascular probe for detection of vulnerable plaque," *Proc. SPIE* **4508**, 88–98 (2001).
6. R. J. Lederman, R. R. Raylman, S. J. Fisher, P. V. Kison, H. San, E. G. Nabel, and R. L. Wahl, "Detection of atherosclerosis using a novel positron-sensitive probe and 18-fluorodeoxyglucose (FDG)," *Nucl. Med. Commun.* **22**(7), 747–753 (2001).
7. R. R. Raylman and R. L. Wahl, "A fiber-optically coupled positron-sensitive surgical probe," *J. Nucl. Med.* **35**(5), 909–913 (1994).
8. M. P. Tornai, C. S. Levin, L. R. MacDonald, C. H. Holdsworth, and E. J. Hoffman, "A miniature phoswitch detector for gamma-ray localization and beta imaging," *IEEE Trans. Nucl. Sci.* **45**(3), 1166–1173 (1998).
9. E. J. Hoffman, M. P. Tornai, C. S. Levin, L. R. MacDonald, and S. Siegel, "Gamma and beta intraoperative probes," *Nucl. Instrum. Methods Phys. Res. A* **392**(A), 324–329 (1997).
10. D. Huang, E. A. Swanson, C. P. Lin, J. S. Schuman, W. G. Stinson, W. Chang, M. R. Hee, T. Flotte, K. Gregory, C. A. Puliafito, and J. G. Fujimoto, "Optical coherence tomography," *Science* **254**, 1178–1181 (1991).
11. A. M. Rollins, M. V. Sivak, S. Radhakrishnan, J. H. Lass, D. Huang, K. D. Cooper, and J. A. Izatt, "Emerging clinical applications of optical coherent tomogaphy," *Opt. Photonics News* **13**(4), 37–41 (Apr. 2002).
12. H. Rashed, J. A. Izatt, and C. Toth, "Optical coherent tomography of the retina," *Opt. Photonics News* **13**(4), 48–51 (Apr. 2002).
13. M. E. Brezinski and J. G. Fujimoto, "Imaging the cardiovascular system with optical coherence tomography," *Opt. Photonics News* **13**(4), 34–35 (Apr. 2002).
14. P. Patwari, N. J. Weissman, S. A. Boppart, C. Jesser, D. Stamper, J. G. Fujimoto, and M. E. Brezinski, "Assessment of coronary plaque with optical coherence tomography and high-frequency ultrasound," *Am. J. Cardiol.* **85**(5), 641–644 (2000).
15. H. Yabushita, B. E. Bouma, S. L. Houser, H. T. Aretz, I. K. Jang, K. H. Schlendorf, C. R. Kauffman, M. Shishkov, D. H. Kang, E. F. Halpern, and G. J. Tearney, "Characterization of human atherosclerosis by optical coherence tomography," *Circulation* **106**(13), 1640–1653 (2002).
16. G. T. Tearney, I. K. Jang, D. H. Kang, H. T. Aretz, S. L. Houser, T. J. Brady, K. Schlendorf, M. Shishkov, and B. E. Bouma, "Porcine coronary imaging in vivo by optical coherent tomography," *Acta Cardiol.* **55**(4), 233–237 (2000).
17. J. M. Schmitt, C. L. Petersen, E. Mont, and R. Virmani, "Imaging and characterization of coronary lesions with optical coherent tomography," *Proc. IEEE Inter. Symp. Biomed. Imaging*, pp. 106–109 (2002).
18. G. J. Tearney, H. Yabushita, S. Houser, H. T. Aretz, Ik-Kyang Jang, K. Schlendorf, C. Kauffmman, M. Shishkov, E. F. Halpern, and B.E. E. Bouma, "Quantification of macrophage content in atherosclerotic plaque by optical coherence tomography," *Circulation* **7**(14), 113–119 (2003).
19. I. K. Jang, B. E. Bouma, D. H. Kang, S. J. Park, S. W. Park, K. B. Seung, K. B. Choi, M. Shishkov, K. Schlendorf, E. Pomerantsev, S. L. Houser, H. T. Aretz, and G. J. Tearney, "Visualization of coronary artherosclerotic plaques in patients using optical coherent tomography: comparison with intravascular ultrasound," *J. Am. Coll. Cardiol.* **39**(4), 604–609 (2002).
20. M. C. Pierce, B. H. Park, B. Cense, and J. F. de Boer, "Simultaneous intensity, birefringence, and flow measurements with high-speed fiber-based optical coherent tomography," *Opt. Lett.* **27**, 1534–1536 (2002).
21. C. E. Saxer, J. F. de Bore, B. H. Park, Y. Zhao, Z. Chen, and J. S. Nelson, "High-speed fiber-based polarization-sensitive optical coherent tomography of *in vivo* human skin," *Opt. Lett.* **25**, 1355–1357 (2000).
22. S. Jiao and L. V. Wang, "Two- dimensional depth-resolved Muellaer matrix of biological tissue measured with double-beam polarization-sensitive optical coherence tomography," *Opt. Lett.* **27**, 101–103 (2002).
23. Z. Chen, T. E. Milner, S. Srinivas, X. Wang, A. Malekafzali, M. J. C. van Germert, and J. S. Nelson, "Noninvasive imaging of in vivo blood flow velocity using optical Doppler tomography," *Opt. Lett.* **22**, 1119–1121 (1997).
24. J. A. Izatt, M. D. Kulkarni, S. Yazdanfar, J. K. Barton, and J. Welch, "*In vivo* bi-directional color Doppler flow imaging of picoliter blood volumes using optical coherence tomography," *Opt. Lett.* **22**, 1439–1441 (1997).
25. T. G. van Leeuwen, M. D. Kulkarni, S. Yazdanfar, A. M. Rollins, and J. A. Izatt, "High-flow-velocity and shear-rate imaging by use of color Doppler optical coherence tomography," *Opt. Lett.* **24**, 1584–1586 (1999).
26. D. Piao, L. L. Otis, N. K. Dutta, and Q. Zhu, "Quantitative assessment of flow velocity estimation algorithms for optical Doppler tomography imaging," *Appl. Opt.* **41**, 6118–6127 (2002).
27. D. Piao, L. L. Otis, and Q. Zhu, "Doppler angle and flow velocity mapping by combining Doppler shift and Doppler bandwidth measurements in optical Doppler tomography," *Opt. Lett.* **28**, 1120–1122 (2003).
28. T. M. Lee, A. L. Oldenburg, S. Sitafalwalla, D. L. Marks, W. Luo, F. J. Toublan, K. S. Suslick, and S. A. Bappart, "Engineered microsphere contrast agents for optical coherence tomography," *Opt. Lett.* **28**, 1546–1548 (2003).
29. K. D. Rao, M. A. Choma, S. Yazdanfar, A. M. Rollins, and J. A. Izatt, "Molecular contrast in optical coherent tomography by use of a pump-probe technique," *Opt. Lett.* **28**, 340–342 (2003).
30. V. V. Tuchin, X. Xu, and R. K. Wang, "Dynamic optical coherence tomography in studies of optical clearing, sedimentation, and aggregation of immersed blood," *Appl. Opt.* **41**, 258–271 (2002).
31. J. K. Barton, F. Guzman, and A. Tumlinson, "Dual modality instrumentation for simultaneous optical coherence tomography imaging and fluorescence spectroscopy," *J. Biomed. Opt.* **9**, 618–623 (2004).
32. Q. Zhu, D. Piao, M. M. Sadeghi, and A. J. Sinusas, "Simultaneous optical coherence tomography imaging and beta particle detection," *Opt. Lett.* **28**, 1704–1706 (2003).
33. D. Piao and Q. Zhu, "Power-efficient grating-based scanning optical delay line: time-domain configuration," *Electron. Lett.* **40**, 97–98 (2004).
34. A. M. Rollins and J. A. Izatt, "Optimal interferometer designs for optical coherence tomography," *Opt. Lett.* **24**, 1484–1486 (1999).
35. G. J. Tearney, S. A. Boppart, B. E. Bouma, M. E. Brezinski, N. J. Weissman, J. F. Southern, and J. G. Fujimoto, "Scanning single-mode fiber optic catheter-endoscope for optical coherence tomography," *Opt. Lett.* **21**, 543–545 (1996).
36. R. C. Fernow, *Introduction to Experimental Particle Physics*, Cambridge University Press (1986).
37. H. Cember, *Introduction to Health Physics*, Pergamon Press, Elmsford, NY (1983).
38. W. F. Libby, "Relation between energy and half-thicknesses for absorption of beta radiation," *Phys. Rev.* **103**, 1900–1901 (1956).
39. C. L. Woody, S. P. Stoll, D. J. Schlyer, M. Gerasimov, P. Vaska, S. Shokouhi, N. Volkow, J. S. Fowler, and S. L. Dewey, "A study of scintillation beta microprobes," *IEEE Trans. Nucl. Sci.* **49**(5), 2208–2212 (2002).